ACS Catalysis

pubs.acs.org/acscatalysis

Research Article

High-Performance Nitrogen-Doped Intermetallic PtNi Catalyst for the Oxygen Reduction Reaction

Xueru Zhao, Cong Xi, Rui Zhang, Liang Song, Chenyu Wang, Jacob S. Spendelow, Anatoly I. Frenkel, Jing Yang,* Huolin L. Xin,* and Kotaro Sasaki*

Cite This: *ACS Catal.* 2020, 10, 10637−10645

Read Online

ACCESS | Metrics & More | Article Recommendations | Supporting Information

ABSTRACT: PtM (M = transition metals) nanomaterials have been recognized as promising catalysts for the oxygen reduction reaction (ORR) in fuel cells, with a much higher performance than pure Pt. However, the insufficient durability issue of PtM is often raised because of the fast dissolution of M in acid, impeding their commercialization. Herein, we report on a Ketjenblack (KB)-supported, nitrogen (N)-doped intermetallic PtNiN (Int-PtNiN/KB) catalyst that exhibits remarkably enhanced ORR activity and stability in an acidic electrolyte, superior to those of disordered PtNi/KB, disordered PtNiN/KB, and commercial Pt/C. The experimental results show that Int-PtNiN/KB has a distinctive ordering structure of alternating Ni_4−N and Pt planes; we attribute the origin of the superior stability of this catalyst to the combined effect of the Ni_4−N formation and the unique intermetallic structure, which effectively precludes Ni dissolution from the core. The density functional theory calculations suggest that the tensile strain introduced by the formation of an intermetallic phase and N-doping optimizes the binding of oxygenated species on the Pt surface and enable highly efficient electron transfer, leading to the enhanced ORR performance. This study offers an appropriate route for further enhancing both the activity and durability of PtM catalysts through a facile synthesis method by annealing in an NH_3 gas under appropriate conditions.

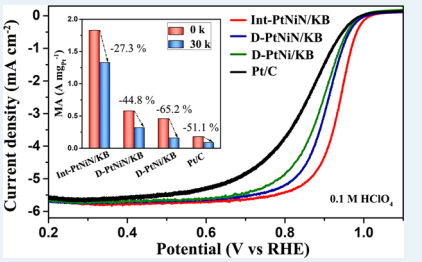

KEYWORDS: *oxygen reduction reaction, intermetallic, core−shell, N-doping, tensile strains*

1. INTRODUCTION

Proton-exchange membrane fuel cells (PEMFCs) are considered as highly promising renewable energy applications because of remarkably high energy conversion efficiency and eco-friendliness.[1−4] However, the commercialization of PEMFCs has been impeded by the cost of Pt-based catalysts for the oxygen reduction reaction (ORR).[5,6] Thus, the essential subject of the current effort is to develop efficient and stable catalysts with minimum consumption of Pt. Many strategies for the formation of low-Pt catalysts, including alloying Pt with 3d transition metals,[7−12] thin Pt shell approaches,[13−19] and the dealloying methods,[20−22] have been reported in previous studies. Particularly, the ordered intermetallic Pt-based catalysts have attracted extensive attention, with much improved activity and durability toward the ORR than the disordered counterpart.[23−29]

Compared to alloy nanoparticles, the ordered intermetallic PtM (M = transition metals) nanocatalysts not only show a stronger atomic interaction between Pt and M for possessing high chemical and structural stability but can also modulate the composition ratio of M to Pt for achieving higher mass activity (MA) for the ORR.[30−34] However, the recent density functional theory (DFT) study shows that both the linear compressional and shear strain effects provided by 3d alloying elements in PtM contribute to the optimal adsorption of the reaction intermediates.[35] Therefore, one plausible strategy for improving the ORR kinetics is by inducing tensile strains within the Pt surface of PtM catalysts. On the other hand, excessive tensile strain may damage the structure of PtM catalysts and even affect the stability of the ORR;[36] hence, regulating the tensile strength is crucial.

Anion doping, such as nitrogen (N)-doping, can be an effective strategy for optimizing the ORR activity and stability of Pt-based catalysts, given that anion dopants tend not only to be incorporated in the catalyst providing optimal strain fields in surface Pt atoms but also to react with selected elements forming chemically stable core compounds. For instance, we have developed highly efficient PtNiN catalysts comprising Pt shells on Ni_4N nitride cores through thermal annealing in an NH_3 gas; the nitride has the bifunctional effect that facilitates the formation of the core−shell structures and improves the performance of the Pt shell by inducing both geometric and electronic effects.[16,37] In addition, a carbon support can very effectively protect catalysts from agglomeration of nanoparticles and increase the conductivity and stability of samples,

Received: July 11, 2020
Revised: August 24, 2020
Published: August 25, 2020

https://dx.doi.org/10.1021/acscatal.0c03036
ACS Catal. 2020, 10, 10637−10645

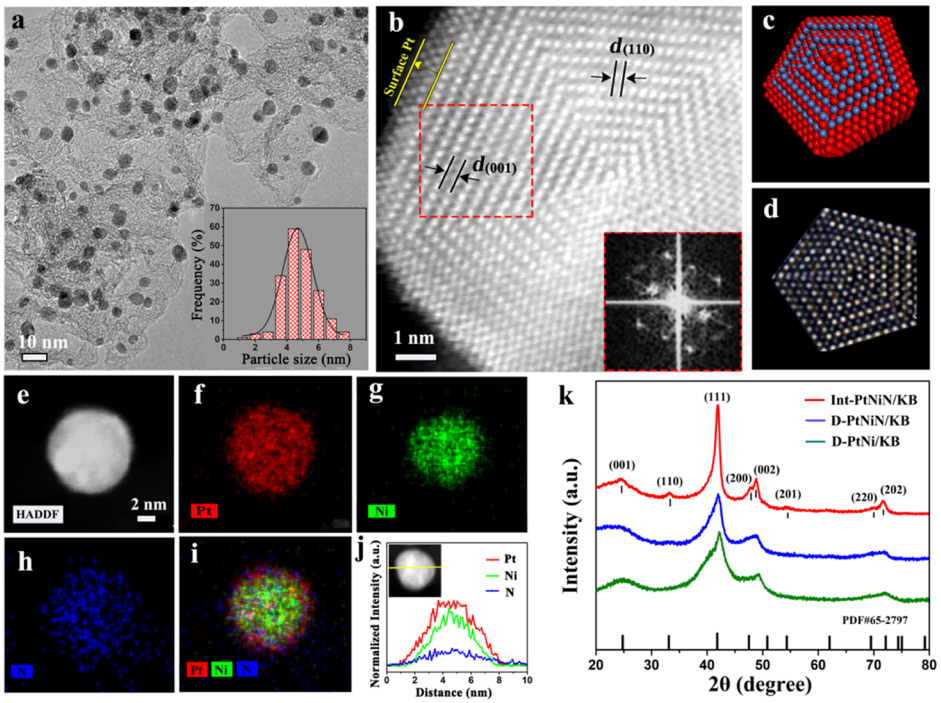

Figure 1. (a) TEM image and particle size distribution (inset) of Int-PtNiN/KB. (b) STEM image of Int-PtNiN/KB with three Pt atoms at the surface. The inset shows the corresponding electron diffraction pattern (indicated by red dashed squares). (c) Schematic of Int-PtNiN/KB with three surface Pt atomic layers, where the red-colored atom is Pt and the blue-colored atom is Ni. (d) Simulated HAADF-STEM image of Int-PtNiN/KB. (e–i) HAADF-STEM image of a single Int-PtNiN/KB particle along with its EDX mapping. (j) EDX elemental line scan across the single Int-PtNiN/KB particle. (k) XRD patterns of Int-PtNiN/KB (9 h, NH_3), D-PtNiN/KB (2 h, NH_3), and D-PtNi/KB (9 h, H_2/Ar) samples annealed at 560 °C.

leading to an optimized electrochemical performance.[38−40] Thus, combining the generation of the intermetallic phases, the anion doping, and selecting an appropriate carbon support can result in a high-activity and high-stability catalyst toward an extraordinary superior ORR performance.

In this work, we report the synthesis of N-doped ordered intermetallic PtNi nanocatalysts supported by Ketjenblack (denoted as Int-PtNiN/KB) with Pt shells *via* a facile synthesis method comprising only one thermal annealing process in an NH_3 gas environment.[41] The MA and specific activity (SA) of Int-PtNiN/KB reach 1.83 A mg_{Pt}^{-1} and 2.92 mA cm^{-2}, respectively, with only a 27% MA loss after 30,000 cycles in an acidic electrolyte, exceeding the DOE 2020 targets on both catalyst activity and durability (0.44 A mg_{Pt}^{-1} in MA and <40% loss in MA after 30,000 cycles). The *in situ* X-ray absorption spectroscopy (XAS) measurements reveal that N-doping caused the formation of a unique core−shell intermetallic structure of Int-PtNiN/KB that enhances the stability of ORR in an acidic solution. Furthermore, as corroborated by DFT calculations, the modest tensile strain (0.2−1.5%) in the ordered Int-PtNiN/KB catalyst is found to be beneficial to the rate increase of the rate-limiting step (from OH* to H_2O) of the ORR as a consequence of the weakening of adsorption of OH* on the Pt surface. These results enable a rational design of highly active and durable intermetallic Pt-based electrocatalysts toward the ORR.

2. RESULTS AND DISCUSSION

2.1. Structure and Morphology Characterization. In general, the formation of ordered intermetallic structure is highly dependent on the annealing temperature and time.[42] The optimized Int-PtNiN/KB nanoparticles with an average size of 4.7 nm and uniform dispersion on the KB support are synthesized by annealing at 560 °C for 9 h under an ammonia gas flow (Figure 1a). The X-ray diffraction (XRD) patterns depict the generation of the ordered intermetallic phase of PtNi, that is, additional peaks at 24.5 and 33.6° corresponded to the (001) and (110) peaks, when the annealing temperature exceeds 500 °C (Figure S1a). The KB support was used because the particle agglomeration during thermal annealing is hampered compared to solid carbon such as Vulcan (Figure S1b). However, excessive temperature will inevitably lead to the aggregation of the nanoparticles with a dramatic increase in particle size even using the KB support and hence adversely affect the activity of the catalyst, as seen in Figure S1c. Meanwhile, the structure transformation from disordered phases to ordered intermetallic phases is also affected by the annealing time (Figure S2). The ordered intermetallic phase of PtNi appears when the annealing time is maintained for more than 5 h at 560 °C. A time−temperature−transformation diagram of the PtNiN system based on the data in Figures S1 and S2 is depicted in Figure S3. The particle sizes of the nanoparticles gradually grow with increasing annealing time at 560 °C (Figure S4). The high-angle annular dark-field scanning transmission electron microscopy (HAADF-STEM) images of the Int-PtNiN/KB nanoparticle illustrate that the core−shell structure is formed with a thin Pt layer (2−3 atom thick) and a core containing Pt and Ni (Figures 1b and S5). The diameter of this nanoparticle is 10.8 nm. The calculated lattice spacings of 0.352 and 0.267 nm from the HAADF-STEM image are ascribed to the (001) and (110) surfaces of the ordered PtNi, respectively, manifesting that the prepared Int-PtNiN/KB nanoparticle has an intermetallic $L1_0$ structure. The corresponding electron diffraction pattern shown in the

https://dx.doi.org/10.1021/acscatal.0c03036
ACS Catal. 2020, 10, 10637−10645

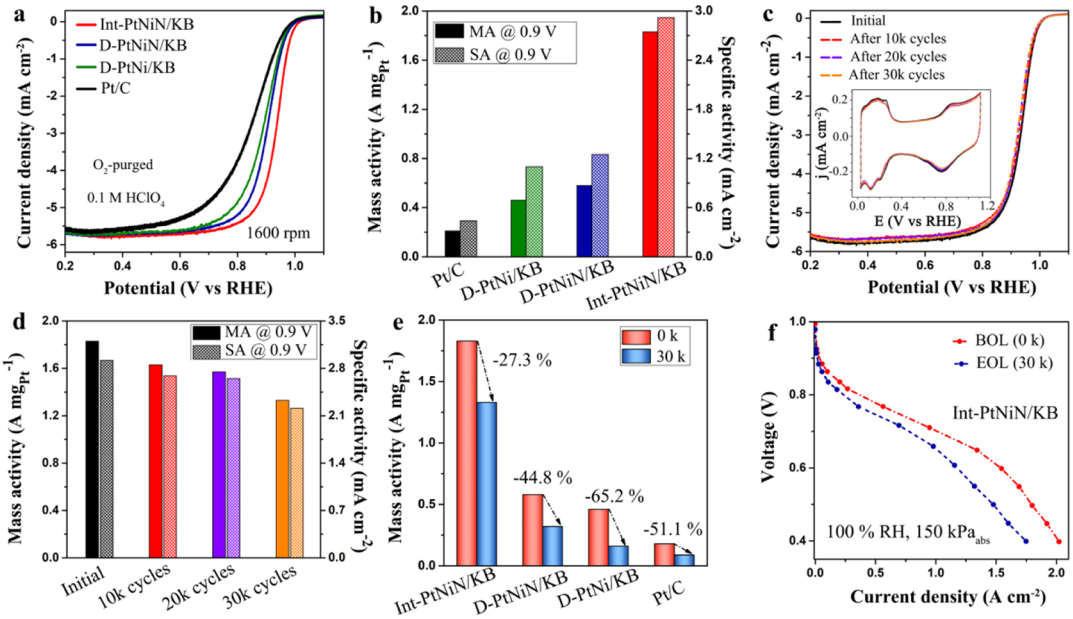

Figure 2. (a) ORR polarization curves of commercial Pt/C, D-PtNi/KB, D-PtNiN/KB, and Int-PtNiN/KB in a 0.1 M $HClO_4$ acidic solution (sweep rate = 10 mV s^{-1}). (b) SA and MA of commercial Pt/C, D-PtNi/KB, D-PtNiN/KB, and Int-PtNiN/KB at 0.9 V. (c) ORR polarization and voltammetry (inset) curves of the Int-PtNiN/KB catalyst before and after different cycle tests between 0.6 and 0.95 V in 0.1 M $HClO_4$. (d) SA and MA of the Int-PtNiN/KB catalyst before and after different cycle tests. (e) MA comparison of Int-PtNiN/KB, D-PtNiN/KB, D-PtNi/KB, and Pt/C before and after 30,000 potential cycles. (f) H_2/air fuel cell polarization curves for the MEA coated with the Int-PtNiN/KB catalyst (the Pt loading is 0.121 mg cm^{-2}), which is recorded under 100% relative humidity at 80 °C, with 150 kPa_{abs} H_2/air.

inset of Figure 1b also demonstrated the formation of an $L1_0$ structure. The atomic model and the simulated HAADF-STEM image of Int-PtNiN/KB nanoparticles were studied to further confirm the above results, as shown in Figure 1c,d; the parameters used in the simulation are consistent with the experimental parameters of the electron microscope. Figure 1d displays the Pt atoms with higher contrast and the Ni atoms with lower contrast in the simulated HAADF-STEM image, which clearly demonstrates a good match between the experimental and simulated images. The energy-dispersive X-ray (EDX) elemental mapping (Figure 1e–i) and the line scanning across a single intermetallic PtNi nanoparticle (Figure 1j) show that the core of Int-PtNiN/KB is surrounded by a thin pure Pt shell and verify the successful doping of N element in the core.

As can be seen from the XRD patterns in Figures 1k and S6, the peak positions of the Int-PtNiN/KB nanocatalyst shift to higher angles than those of commercial Pt/C (Figure S6) but are located at lower angles than those of disordered PtNiN/KB (denoted as D-PtNiN/KB). Disordered PtNi/KB (denoted as D-PtNi/KB) showed the largest peak shifts to higher angles among the catalysts examined. This observation clearly demonstrates that alloying Pt with Ni induces the significant contraction in Pt bonding (D-PtNi/KB) compared to Pt/C because of the shorter bond length of Ni; however, the N-dopants reduce the contraction (D-PtNiN/KB) and the formation of intermetallic phase further lowers the contraction. In other words, tensile strain is introduced in D-PtNi/KB by the N-dopants and the transformation to the ordered structure, which is the key cause of increased activity of the Int-PtNiN/KB catalyst. Having two important effects, it opens possibility to improve the catalytic activity for a large range of catalysts. The lattice constant can be calculated *via* the Scherrer equation based on the XRD patterns. The lattice contractions of D-PtNiN/KB and D-PtNi/KB are 5.09 and 5.88%, respectively, compared to the commercial Pt/C, while the lattice contraction of Int-PtNiN/KB catalyst is 4.84% for *a* and *b* (Table S1). Interestingly, the lattice constant *c* in a unit cell along the *z* reduces with the structure transformation from a disordered structure to an ordered intermetallic structure, which is similar to the theoretical changes of lattice constant from disordered PtNi (PDF# 65-9445) to ordered intermetallic PtNi (PDF# 65-2797). In comparison with D-PtNiN/KB, the lower lattice contraction degree of the Int-PtNiN/KB catalyst may result in the weaker interaction between surface Pt and reactants, thus impairing the adsorption of intermediates on Pt surface and, in turn, accelerating the whole ORR process.[31]

2.2. ORR and Membrane Electrode Assembly Performance of Int-PtNiN/KB. The ORR electrocatalytic performance of as-prepared catalysts was evaluated by polarization curves obtained using the ring disk electrode (RDE) in an O_2-saturated 0.1 M $HClO_4$ electrolyte with a sweep rate of 10 mV s^{-1} and a rotation speed of 1600 rpm at room temperature (Figure 2a). The Int-PtNiN/KB catalyst exhibits a half-wave potential ($E_{1/2}$) of 935 mV, which is more positive than those of D-PtNiN/KB (908 mV) and D-PtNi/KB (890 mV), indicating superior kinetics for the ORR on the Int-PtNiN/KB catalyst (Table S2). In general, the cyclic voltammetry (CV) curves of Int-PtNiN/KB, D-PtNiN/KB, D-PtNi/KB, and commercial Pt/C catalysts were first measured in an Ar-purged 0.1 M $HClO_4$ solution at a sweep rate of 20 mV s^{-1} (Figure S7). The electrochemical surface area (ECSA) of Int-PtNiN/KB calculated from averaged hydrogen (H) adsorption and desorption peaks is 62.6 m^2 g^{-1}, which is much higher than those of commercial Pt/C (47.8 m^2 g^{-1}), D-PtNiN/KB (46.3 m^2 g^{-1}), and D-PtNi/KB (42.0 m^2 g^{-1}). CO stripping was also employed to evaluate the ECSA of the Int-PtNiN/KB catalyst (Figure S8), which is larger than that from the underpotentially adsorbed hydrogen (H_{upd}) method (85.9

https://dx.doi.org/10.1021/acscatal.0c03036
ACS Catal. 2020, 10, 10637−10645

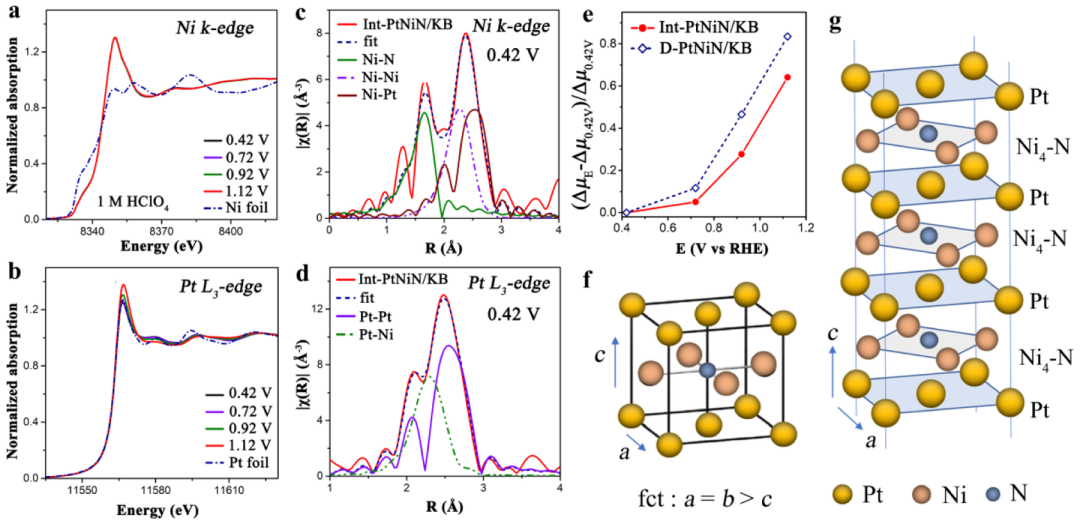

Figure 3. *In situ* (a) Ni K-edge XANES of Int-PtNiN/KB at different applied potentials with a Ni foil and (b) Pt L_3-edge XANES of Int-PtNiN/KB at different applied potentials with a Pt foil. *In situ* (c) Ni K-edge FT-EXAFS spectrum at 0.42 V with a first-shell fit together with Ni−Ni, Ni−Pt, and Ni−N contributions and (d) Pt L_3-edge FT-EXAFS spectrum at 0.42 V with a first-shell fit together with Pt−Pt and Pt−Ni contributions of Int-PtNiN/KB. The *in situ* data were collected in a 1 M $HClO_4$ electrolyte using an electrochemical cell. (e) Comparison of the change of the Pt adsorption edge peaks ($\Delta\mu$) of the XANES spectra (relative to $\Delta\mu$ at 0.42 V) for Int-PtNiN/KB and D-PtNiN/KB as a function of potential obtained in 1 M $HClO_4$. (f) $L1_0$-type structure with a nitrogen atom at the center of fct (*N* of Ni−N is 4). (g) Schematic of the ordering structure alternating Ni_4−N moieties and Pt planes.

vs 62.6 m^2 g^{-1}), possibly because of a suppression effect of sublayer Ni on H_{upd}.[43,44] The ORR polarization curves of Int-PtNiN/KB, D-PtNiN/KB, D-PtNi/KB, and Pt/C samples at different rotation rates as well as the corresponding Koutecký−Levich (K−L) plots are provided in Figure S9. Based on the K−L plots at different potentials, the number of transferred electrons (n) of Int-PtNiN/KB, D-PtNiN/KB, and D-PtNi/KB are calculated to be about 4, which is the same as that of commercial Pt/C, illustrating that KB-supported PtNi nanocatalysts favors a $4e^-$ oxygen reduction process, whether in ordered or disordered form. MA and SA are practical indicators for evaluating the intrinsic activity of ORR catalysts. After normalizing over Pt mass, Figure 2b describes the MA of 0.18, 0.46, 0.58, and 1.83 A mg_{Pt}^{-1} at 0.9 V on commercial Pt/C, D-PtNi/KB, D-PtNiN/KB, and Int-PtNiN/KB, respectively. The MA of Int-PtNiN/KB is the highest among the catalysts examined, which is 10.1 times higher than that of Pt/C. Meanwhile, the SA of Int-PtNiN/KB reaches 2.92 mA cm^{-2}, which is a 7.7-fold enhancement in comparison with Pt/C (0.38 mA cm^{-2}). Interestingly, even with their smaller ECSA, the SAs of D-PtNiN/KB and D-PtNi/KB are more than 3-fold and 2-fold higher than that of Pt/C, respectively. Clearly, the Int-PtNiN/KB nanocatalysts possess the best ORR activity compared to the D-PtNiN/KB and D-PtNi/KB catalysts as well as Pt/C, which can be attributed to optimized adsorption strength by strains induced in surface Pt atoms arising from the synergies of N-doped and the distinct intermetallic structure as discussed below.

Accelerated durability test (ADT) was conducted at potentials between 0.6 and 0.95 V (holding for 3 s at each potential) to evaluate the durability of catalysts. Even after 30,000 ADT cycles, the polarization curves of Int-PtNiN/KB exhibit a negligible shift, demonstrating an excellent long-term stability toward the ORR activity (Figure 2c). On the other hand, D-PtNiN/KB and D-PtNi/KB show 20 mV and 69 mV decay of $E_{1/2}$, respectively (Figure S10). The ECSA of Int-PtNiN/KB at end-of-life (EOL) (60.3 m^2 g^{-1}), which is calculated from H adsorption/desorption regions in the CV curves (the inset in Figure 2c), shows a loss of only 3.7% compared to that at the beginning-of-life (BOL), as presented in Table S3. The loss in the ECSA of Int-PtNiN/KB is substantially smaller than those of D-PtNiN/KB (12.5%), D-PtNi/KB (17.1%), and Pt/C (27.6%) (Table S4). Furthermore, the Int-PtNiN/KB catalyst shows only 27.3% drop in MA at EOL (Figure 2d), contrasting with large decreases of 44.8% for the D-PtNiN/KB catalyst, 65.2% for the D-PtNi/KB catalyst, and 51.1% for commercial Pt/C (Figure 2e). Notably, the retained MA for the Int-PtNiN/KB catalyst at EOL (1.33 A mg_{Pt}^{-1}) is still 7.4 times greater than that of pristine Pt/C catalyst. Similar to changes in MA at EOL, the loss of SA of Int-PtNiN/KB (24.3%) is much lower than that of the D-PtNiN/KB catalyst (36.8%), D-PtNi/KB (58.2%), and commercial Pt/C (33.3%) (Table S4). Excitingly, the transmission electron microscopy (TEM) image of Int-PtNiN/KB after 30k cycles illustrates the limited agglomeration of the nanoparticles (Figure S11a), which indicates that the KB supports inhibit the agglomeration or growth of catalysts during the ORR process. The measurements of EDX spectra for the Int-PtNiN/KB sample after 30k ADT cycles clearly demonstrate that a reasonably sufficient amount of Ni is remained at the center of the nanoparticles (Figure S11), which is much higher than that of D-PtNiN/KB (Table S5). As we expected, the N-doping and the formation of an intermetallic phase are significantly profitable to impart the stability of PtNi catalysts by impeding the diffusivity of Ni in the core as discussed below and also the thin Pt outer shells effectively suppress the leaching of Ni atoms to an acidic electrolyte during the catalytic reactions.

To further corroborate the superior ORR activity revealed by RDE results, membrane electrode assembly (MEA) performance and durability of Int-PtNiN/KB were evaluated using the DOE protocols. The H_2/air polarization curve of Int-PtNiN/KB at BOL in Figure 2f delivers a current density of 1550 mA cm^{-2} at 0.6 V, which outperforms most of the Pt-

https://dx.doi.org/10.1021/acscatal.0c03036
ACS Catal. 2020, 10, 10637−10645

based catalysts reported in recently published papers, considering comparable Pt loadings (Table S6). Moreover, the current density at 0.8 V is 348 mA cm^{-2}, exceeding the DOE target of 300 mA cm^{-2}. The excellent performance in both the kinetic and Ohmic regions can be attributed to the high intrinsic activity of intermetallic PtNiN nanoparticles and the well-controlled particle dispersion on carbon support. The MA of the Int-PtNiN/KB catalyst measured under 0.9 V at BOL is 0.49 A mg_{Pt}^{-1} (Figure S12). After the ADT, the MA of Int-PtNiN/KB was maintained at a high level of 0.32 A mg_{Pt}^{-1}, above the DOE target for EOL (0.264 A mg_{Pt}^{-1}). Furthermore, the loss in MA after the ADT is 35%, which also meets the DOE requirement of less than 40% loss. The voltage loss at 0.8 A cm^{-2} and the ECSA loss after the ADT are presented in Table S7. The Int-PtNiN/KB catalyst exhibits a voltage drop of 32 mV at 0.8 A cm^{-2} (from 729 to 697 mV), which is only slightly higher than the DOE target of 30 mV or less. The ECSA losses after the ADT (50 and 41% by H and CO stripping methods, respectively) are higher than that obtained from the RDE measurement, primarily because of the more corrosive environment in the fuel cell operation. These MEA results demonstrate excellent potentials of Int-PtNiN/KB as a practical fuel cell catalyst.

2.3. *In Situ* XAS Analysis of Int-PtNiN/KB. *In situ* XAS was employed to evaluate the oxidation susceptibility and the structural properties of the Int-PtNiN/KB catalysts. Figure 3a shows the *in situ* X-ray absorption near-edge structure (XANES) spectra for Ni K-edge of Int-PtNiN/KB nanoparticles in a 1 M $HClO_4$ electrolyte at various potentials. The difference of the Ni K-edge XANES spectra between Int-PtNiN/KB and a reference Ni foil suggests that the electronic and structural properties of Ni have been modified by N-doping and alloying with Pt. As shown in Figure S13a,b, extended X-ray absorption fine structure (EXAFS) spectra, shown in *k*-space and *r*-space, respectively, also demonstrate that the nearest atomic environment of Ni in Int-PtNiN/KB is very different from that in a Ni foil. Furthermore, no obvious changes of Ni K-edge XANES are observed in a potential range of 0.42−1.12 V (Figure 3a), consistent with the fact that the Pt shell protects the Ni from being dissolved/oxidized during the ORR process. Correspondingly, the Fourier transform (FT) magnitude of the Ni K-edge EXAFS (FT-EXAFS) of Int-PtNiN/KB further proves that the intermetallic structure of Int-PtNiN/KB nanoparticles is very stable because no discernible change in atomic structure at different potentials is seen (Figure S13b).

The *in situ* XANES spectra of the Pt L_3-edge from the Int-PtNiN/KB catalyst at different potentials are shown in Figure 3b, together with that of a Pt reference foil. In general, the intensity of white lines (first peaks of Pt L_3 XANES) rises with increasing potentials as a consequence of depleting Pt's d-band because of the formation of Pt oxide.[45−47] The XANES spectra of Int-PtNiN/KB also show an increase in white line intensity (as well as an increase in peak intensity at 1.6 Å in FT-EXAFS of Int-PtNiN/KB with increasing potentials as depicted in Figure S13d); however, the degree of potential dependence observed for Int-PtNiN/KB is smaller than that observed for D-PtNiN/KB (Figure S14d). The effect is more clearly seen in Figure 3e, which shows relative changes in white line intensity $((\Delta\mu_E - \Delta\mu_{0.42V})/\Delta\mu_{0.42V})$ from that at 0.42 V plotted versus applied potentials. This provides clear evidence of enhanced stability of Pt in the Int-PtNiN/KB catalyst, which occurred, as we hypothesize, because of the formation of intermetallic structure, in comparison with the D-PtNiN/KB catalysts. We also emphasize that this inhibiting effect on Pt oxidation enhances the ORR activity because more metallic Pt atoms on the surface are retained as active sites at increasing potentials.

The results of concurrent fitting for the Ni K-edge and Pt L_3-edge data of the Int-PtNiN/KB catalyst at a potential of 0.42 V are shown in Figure 3c,d. There is good agreement between the fits and the experimental spectra. Also shown are Ni−Ni, Ni−Pt, and Ni−N contributions for the Ni edge data fitting and Pt−Pt and Pt−Ni contributions for the Pt edge data fitting. The fitting for the Ni K-edge and Pt L_3-edge data from the D-PtNiN/KB catalyst at a potential of 0.42 V is shown in Figure S14c,f, respectively. The best fit results for coordination numbers (N), bond lengths (d), and bond length disorder parameters (σ^2) from Int-PtNiN/KB and D-PtNiN/KB catalysts are summarized in Tables S8 and S9.

The coordination number N of Pt−Pt pairs for Int-PtNiN/KB is determined to be 5.9 ± 0.3 (Table S8). Our previous EXAFS analysis of Pt/Pd/C catalysts (the average particle size is 4.2 nm) comprising Pt monolayer shells on Pd nanoparticles showed that the N of Pt−Pt was 5.8 (±0.8), which is close to the number obtained from the present fitting. Figure S15 shows the coordination numbers of surface−surface (ss) atoms (N_{ss}) for icosahedra (ICO) and cuboctahedra (CUBO) (which are considered as typical structures of Pt-based nanoparticles)[48] calculated from a theoretical nanocluster model as a function of particle size.[49,50] The N_{ss} numbers for a particle size of 4.7 nm are 5.9 and 4.8 for ICO and CUBO, respectively, and the average is 5.4. (We note that the N_{ss} number for an ideal and infinite Pt(111) crystal plane is 6.) Taking into account that (i) the cores of the Int-PtNiN/KB catalyst have mixed Ni and Pt atoms and (ii) Pt atoms in the surface monolayer may coordinate with Pt atoms in the cores (forming multilayers), the N of Pt−Pt for the Int-PtNiN/KB catalyst may be higher than the value of 5.4. Therefore, the Pt−Pt coordination number value (5.9 ± 0.3) obtained by the present fitting is consistent with the formation of thin Pt shells.

Another intriguing feature is the N of Ni−N for Int-PtNiN/KB, which is determined to be 3.2 ± 0.5 as listed in Table S8. The N of Ni−N for a $L1_0$-type structure with a nitrogen atom at a center of a face-centered tetragonal (fct) structure is 4 (Ni_4−N as shown in Figures 3f and S16c), which is close to the EXAFS fitting result. The N of Ni−N for D-PtNiN/KB from the EXAFS fitting is 4.4 ± 0.9 (Table S9), which is higher than that of Int-PtNiN/KB, consistent with the observed high intensity of Ni−N contribution in the fitting in Figure S14c (indicated by a green curve with a circle). A combination of this increase in the coordination number of Ni−N bonds and the absence of the intermetallic phase signatures in the XRD pattern (Figure 1k) of D-PtNiN/KB leads to a hypothesis that D-PtNiN/KB has a disordered fcc phase (Figure S16a) containing Ni atoms at face centers (Figure S16b). Such a phase has a higher Ni−N coordination number (N = 6) compared to the intermetallic phase (N = 4). The overall decrease in the measured coordination numbers of Ni−N bonds compared to their values in the idealized models of the intermetallic and disordered fcc phases is likely caused by the surface truncation effect of the nanoparticles, as explained in great detail in the Supporting Information. During the longer annealing period (9 h) at 560 °C, we consider that the atomic ordering toward the $L1_0$-type intermetallic structure takes place, thereby leading to a decrease in the N of Ni−N for Int-PtNiN/KB. This notion is also supported by a change in bond

https://dx.doi.org/10.1021/acscatal.0c03036
ACS Catal. 2020, 10, 10637−10645

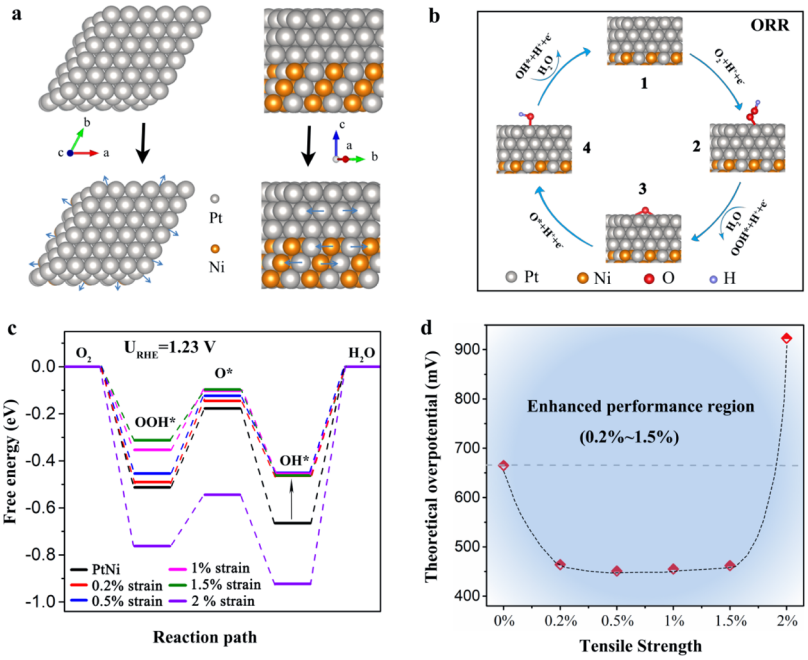

Figure 4. (a) Schematic of the ordered PtNi without tensile strains and ordered PtNi with tensile strains introduced by N-doping, where the gray-colored atom is Pt and the orange-colored atom is Ni. (b) ORR mechanisms of Int-PtNiN/KB. The Pt, Ni, O, and H are labeled as gray, orange, red, and purple, respectively. (c) Free energy diagram calculated *via* the DFT method on the associative pathway for different tensile strains on the ordered PtNi surface. (d) Theoretical overpotential as a function of tensile strength on the ordered PtNi surface.

length disorder parameter (σ^2), which represents the degree of disorder (and resultant strains) in alloys.[51] The σ^2 of D-PtNiN/KB is 0.0123 ± 0.0043 Å^2 (Table S9) and that of Int-PtNiN/KB (0.0106 ± 0.0022 Å^2 in Table S8) is lower than that of D-PtNiN/KB. The decrease in σ^2 is consistent with the formation of an ordered $L1_0$ intermetallic phase in Int-PtNiN/KB (Figure S16c).

As discussed above, the *in situ* XAS measurements reveal the unique intermetallic structure of Int-PtNiN/KB, which consists of alternating atomic layers of a Ni_4−N moiety and a Pt plane along the [001] direction (the *c*-axis), as shown in Figure 3g. Some metal−nitrogen moieties such as Fe−N_x are known to be catalytically active and chemically durable in acidic solutions.[52−54] The formation of a stable Ni−N bonding due to N-doping could enhance the stability of the D-PtNiN/KB catalyst compared to that of the D-PtNi/KB catalyst, as shown in Figure 2e, which is in line with our previous studies.[16,36] The N atom is considered to have the pinning effect to the surrounding Ni atoms. In the present investigation, we observed the significantly higher stability of Int-PtNiN/KB compared to that of D-PtNiN/KB after 30,000 potential cycles (Figure 2e). Although the Ni_4−N moieties are not subject to the electrolyte and thus are not involved in reaction, the ordered structure of alternating Ni_4−N and Pt planes must be the origin of the superior durability of this catalyst. We envisage that, in addition to the pinning effect due to the chemically durable Ni−N bonding, the intermetallic structure further impedes the diffusivity of Ni atoms because every Ni_4−N moiety is sandwiched by Pt planes, which results in considerable inhibition of dissolving Ni atoms from the core. This finding offers a new opportunity to resolve longstanding challenges to suppress the dissolution of M atoms and further enhance the stability of PtM catalysts for the ORR through a very simple synthesis method, that is, annealing in an NH_3 gas under appropriate temperature and time. The doped N in Int-PtNiN/KB also has another beneficial effect to enhance the ORR activity, which is discussed based on DFT calculations in the next section.

2.4. DFT Analysis. The XRD measurements demonstrated that the lattice contraction compared to that of Pt/C decreases in the following order: D-PtNi/KB (5.88%) > D-PtNiN/KB (5.09%) > Int-PtNiN/KB (4.84%) (Table S1). On the other hand, the order of the ORR activity (MA and SA) is opposite (Int-PtNiN/KB > D-PtNiN/KB > D-PtNi/KB) (Figure 2b). One may consider that the high lattice contraction caused by alloying Pt with Ni is alleviated by tensile strains because of the N-doping and the structural ordering, resulting in the optimum adsorption strength and the resultant enhanced ORR activity. To prove this hypothesis, DFT calculations were implemented to explore the effects of tensile strains on the enhanced ORR performance of the ordered intermetallic PtNi catalyst. As shown in Figure 4a, the tensile strains introduced by N-doping are applied by expanding the lattice length in the *x* and *y* directions in the Pt(111) surface of the ordered PtNi (see the Supporting Information for more details). Commonly, the ORR takes an associative four-electron pathway in an acidic solution (Figure 4b), which starts with the adsorption of O_2, followed by the formation of the reaction intermediates, that is, OOH*, O*, and OH*, and goes back to the initial state for the new cycle after the production of H_2O.[55,56] Based on this mechanism, a series of tension values (0, 0.2, 0.5, 1, 1.5, and 2%) were exploited on the ordered PtNi(111) and the corresponding Gibbs free energy (ΔG) for the ORR of various tensile structures was calculated (Table S10).

Figure 4c presents the comparison of Gibbs free energy and the theoretical overpotential of ordered PtNi catalysts with various tensile structures, computed at the equilibrium potential (U = 1.23 V). The overpotential (η) depends on the step having the maximum uphill change in free energy, so the rate-limiting reaction for this system is the last reduction

https://dx.doi.org/10.1021/acscatal.0c03036
ACS Catal. 2020, 10, 10637−10645

step from OH* to H_2O. The DFT results indicate that the over strong adsorption of OH* will cause the potential-demanding step and the optimum tensile strength range (0.2−1.5%) can weaken the adsorption of all intermediates, especially for OH*, reducing the energy barriers for the formation of H_2O. Linear relationships between the theoretical overpotential and the various tensile strains on the ordered PtNi were established to achieve a better understanding for the effect of tensile strains on the ORR process. As displayed in Figure 4d, the theoretical overpotential obviously decreases with the augment of tensile strength and the optimal tensile strain range is from 0.2 to 1.5%; in contrast, excess tensile strains will result in higher overpotential for ordered PtNi. Noteworthy, the adsorption of OH* is reduced by 0.21 eV when 0.5% tensile strain is introduced in the structure (as indicated by an arrow in Figure 4c), leading to the 214 mV reduction of the overpotential (from 665 to 415 mV). Overall, the enhanced ORR activity on Int-PtNiN/KB can be attributed to the impact of the surface strain caused by N-doping, which is consistent with the experimental results. The moderate tensile strains will adjust binding of intermediates on the strained Pt overlayer surface; this enables highly efficient electron transfer during catalysis processes and consequently reduces overpotentials, thereby leading to the enhancement of the ORR activity of Int-PtNiN/KB.

3. CONCLUSIONS

In summary, we have synthesized the N-doped and structurally ordered Int-PtNiN/KB core−shell nanoparticles as ORR catalysts by tuning the annealing temperature and time. The optimized Int-PtNiN/KB shows the superior ORR activity and durability by RDE tests compared to the D-PtNiN/KB, D-PtNi/KB, and commercial Pt/C. The MA and SA of Int-PtNiN/KB are 1.83 A mg_{Pt}^{-1} and 2.92 mA cm^{-2} at 0.9 V, which are 10.1-fold and 7.7-fold as high as the commercial Pt/C, respectively. In MEA testing, Int-PtNiN/KB meets the DOE targets for MA, loss in MA after ADT, and performance at 0.8 V. The *in situ* XAS reveals the formation of a unique ordered structure of alternately stacked Ni_4−N moieties and Pt layers along the [001] direction, which could be the origin of the enhanced stability of Int-PtNiN/KB. The DFT simulations indicate that the optimal strains induced by the synergy between the N-doping and the formation of intermetallic phase result in optimizing the binding of intermediates on the strained Pt surface, thus facilitating electron-transfer processes and enhancing the intrinsic ORR activity. This work provides an effective direction to resolve longstanding challenges to improve the intrinsic activity and stability of binary or even ternary Pt-based electrocatalysts for the ORR.

■ ASSOCIATED CONTENT

Supporting Information

The Supporting Information is available free of charge at https://pubs.acs.org/doi/10.1021/acscatal.0c03036.

Material synthesis and characterizations, measurements, and DFT calculations (PDF)

■ AUTHOR INFORMATION

Corresponding Authors

Jing Yang − *Institute of New-Energy Materials, Key Laboratory of Advanced Ceramics and Machining Technology of Ministry of Education, School of Materials Science and Engineering, Tianjin University, Tianjin 300072, China*; Email: yang_jing@tju.edu.cn

Huolin L. Xin − *Department of Physics and Astronomy, University of California, Irvine, California 92697, United States*; orcid.org/0000-0002-6521-868X; Email: huolinx@uci.edu

Kotaro Sasaki − *Chemistry Department, Brookhaven National Laboratory, Upton, New York 11973, United States*; orcid.org/0000-0003-2474-8323; Email: ksasaki@bnl.gov

Authors

Xueru Zhao − *Chemistry Department, Brookhaven National Laboratory, Upton, New York 11973, United States; Institute of New-Energy Materials, Key Laboratory of Advanced Ceramics and Machining Technology of Ministry of Education, School of Materials Science and Engineering, Tianjin University, Tianjin 300072, China*

Cong Xi − *Institute of New-Energy Materials, Key Laboratory of Advanced Ceramics and Machining Technology of Ministry of Education, School of Materials Science and Engineering, Tianjin University, Tianjin 300072, China*

Rui Zhang − *Department of Physics and Astronomy, University of California, Irvine, California 92697, United States*

Liang Song − *Chemistry Department, Brookhaven National Laboratory, Upton, New York 11973, United States*

Chenyu Wang − *Materials Physics and Application Division, Los Alamos National Laboratory, Los Alamos, New Mexico 87545, United States*

Jacob S. Spendelow − *Materials Physics and Application Division, Los Alamos National Laboratory, Los Alamos, New Mexico 87545, United States*

Anatoly I. Frenkel − *Chemistry Department, Brookhaven National Laboratory, Upton, New York 11973, United States; Department of Materials Science and Chemical Engineering, Stony Brook University, Stony Brook, New York 11794, United States*

Complete contact information is available at: https://pubs.acs.org/10.1021/acscatal.0c03036

Notes

The authors declare no competing financial interest.

■ ACKNOWLEDGMENTS

This manuscript has been authored by the employees/guests of Brookhaven Science Associates, LLC, under contract no. DE-SC0012704 with the U.S. Department of Energy. The publisher by accepting the manuscript for publication acknowledges that the United States Government retains a nonexclusive, paid-up, irrevocable, worldwide license to publish or reproduce the published form of this manuscript, or allows others to do so, for United States Government purposes. EXAFS analysis and modeling of Ni−Pt interactions by A.I.F. were supported as part of the Integrated Mesoscale Architectures for Sustainable Catalysis (IMASC), an Energy Frontier Research Center funded by the U.S. Department of Energy, Office of Science, Basic Energy Sciences under Award DE-SC0012573. This research used resources of the Center for Functional Nanomaterials and the QAS beamline (7-BM) of the National Synchrotron Light Source II, which are U.S. DOE Office of Science Facilities, at the Brookhaven National Laboratory under contract no. DE-SC0012704. QAS beamline operations were supported in part by the Synchrotron Catalysis Consortium (U.S. DOE, Office of Basic Energy Sciences,

https://dx.doi.org/10.1021/acscatal.0c03036
ACS Catal. 2020, 10, 10637−10645

Grant no. DE-SC0012335). MEA testing at LANL was supported by the U.S. Department of Energy, Energy Efficiency and Renewable Energy, Fuel Cell Technologies Office and by LANL's Laboratory Directed Research and Development (LDRD) program under project number 20190640PRD3. We thank Dr Radoslav R. Adzic for constructive discussion. R.Z. was supported by the startup funding of H.L.X.

REFERENCES

(1) Debe, M. K. Electrocatalyst Approaches and Challenges for Automotive Fuel Cells. *Nature* **2012**, *486*, 43−51.
(2) Miao, Z.; Wang, X.; Tsai, M. C.; Jin, Q.; Liang, J.; Ma, F.; Wang, T.; Zheng, S.; Hwang, B. J.; Huang, Y.; Guo, S.; Li, Q. Atomically Dispersed Fe-N_x/C Electrocatalyst Boosts Oxygen Catalysis via a New Metal-Organic Polymer Supramolecule Strategy. *Adv. Energy Mater.* **2018**, *8*, 1801226.
(3) Mazumder, V.; Lee, Y.; Sun, S. Recent Development of Active Nanoparticle Catalysts for Fuel Cell Reactions. *Adv. Funct. Mater.* **2010**, *20*, 1224−1231.
(4) Cano, Z. P.; Banham, D.; Ye, S.; Hintennach, A.; Lu, J.; Fowler, M.; Chen, Z. Batteries and Fuel Cells for Emerging Electric Vehicle Markets. *Nat. Energy* **2018**, *3*, 279−289.
(5) Liu, M.; Zhao, Z.; Duan, X.; Huang, Y. Nanoscale Structure Design for High-Performance Pt-Based ORR Catalysts. *Adv. Mater.* **2019**, *31*, 1802234.
(6) Tian, X.; Luo, J.; Nan, H.; Zou, H.; Chen, R.; Shu, T.; Li, X.; Li, Y.; Song, H.; Liao, S.; Adzic, R. R. Transition Metal Nitride Coated with Atomic Layers of Pt as a Low-cost, Highly Stable Electrocatalyst for the Oxygen Reduction Reaction. *J. Am. Chem. Soc.* **2016**, *138*, 1575−1583.
(7) Gao, L.; Li, X.; Yao, Z.; Bai, H.; Lu, Y.; Ma, C.; Lu, S.; Peng, Z.; Yang, J.; Pan, A.; Huang, H. Unconventional p-d Hybridization Interaction in PtGa Ultrathin Nanowires Boosts Oxygen Reduction Electrocatalysis. *J. Am. Chem. Soc.* **2019**, *141*, 18083.
(8) Lai, W. H.; Zhang, B. W.; Hu, Z.; Qu, X. M.; Jiang, Y. X.; Wang, Y. X.; Wang, J. Z.; Liu, H. K.; Chou, S. L. The Quasi-Pt-Allotrope Catalyst: Hollow PtCo@single-Atom Pt_1 on Nitrogen-Doped Carbon toward Superior Oxygen Reduction. *Adv. Funct. Mater.* **2019**, *29*, 1807340.
(9) Cao, L.; Zhao, Z.; Liu, Z.; Gao, W.; Dai, S.; Gha, J.; Xue, W.; Sun, H.; Duan, X.; Pan, X.; Mueller, T.; Huang, Y. Differential Surface Elemental Distribution Leads to Significantly Enhanced Stability of PtNi-Based ORR Catalysts. *Matter* **2019**, *1*, 1567−1580.
(10) Lim, J.; Shin, H.; Kim, M.; Lee, H.; Lee, K.-S.; Kwon, Y.; Song, D.; Oh, S.; Kim, H.; Cho, E. Ga-Doped Pt-Ni Octahedral Nanoparticles as a Highly Active and Durable Electrocatalyst for Oxygen Reduction Reaction. *Nano Lett.* **2018**, *18*, 2450−2458.
(11) Beermann, V.; Gocyla, M.; Willinger, E.; Rudi, S.; Heggen, M.; Dunin-Borkowski, R. E.; Willinger, M.-G.; Strasser, P. Rh-Doped Pt-Ni Octahedral Nanoparticles: Understanding the Correlation between Elemental Distribution, Oxygen Reduction Reaction, and Shape Stability. *Nano Lett.* **2016**, *16*, 1719−1725.
(12) Chung, D. Y.; Jun, S. W.; Yoon, G.; Kwon, S. G.; Shin, D. Y.; Seo, P.; Yoo, J. M.; Shin, H.; Chung, Y.-H.; Kim, H.; Mun, B. S.; Lee, K.-S.; Lee, N.-S.; Yoo, S. J.; Lim, D.-H.; Kang, K.; Sung, Y.-E.; Hyeon, T. Highly Durable and Active PtFe Nanocatalyst for Electrochemical Oxygen Reduction Reaction. *J. Am. Chem. Soc.* **2015**, *137*, 15478−15485.
(13) Kuttiyiel, K. A.; Sasaki, K.; Choi, Y.; Su, D.; Liu, P.; Adzic, R. R. Bimetallic IrNi Core Platinum Monolayer Shell Electrocatalysts for the Oxygen Reduction Reaction. *Energy Environ. Sci.* **2012**, *5*, 5297−5304.
(14) Sasaki, K.; Naohara, H.; Cai, Y.; Choi, Y. M.; Liu, P.; Vukmirovic, M. B.; Wang, J. X.; Adzic, R. R. Core-protected Platinum Monolayer Shell High-stability Electrocatalysts for Fuel-cell Cathodes. *Angew. Chem., Int. Ed.* **2010**, *49*, 8602−8607.
(15) He, D. S.; He, D.; Wang, J.; Lin, Y.; Yin, P.; Hong, X.; Wu, Y.; Li, Y. Ultrathin Icosahedral Pt-Enriched Nanocage with Excellent Oxygen Reduction Reaction Activity. *J. Am. Chem. Soc.* **2016**, *138*, 1494−1497.
(16) Kuttiyiel, K. A.; Choi, Y.; Hwang, S.-M.; Park, G.-G.; Yang, T.-H.; Su, D.; Sasaki, K.; Liu, P.; Adzic, R. R. Enhancement of the Oxygen Reduction on Nitride Stabilized Pt-M (M=Fe, Co, and Ni) Core-shell Nanoparticle Electrocatalysts. *Nano Energy* **2015**, *13*, 442−449.
(17) Sasaki, K.; Naohara, H.; Choi, Y.; Cai, Y.; Chen, W. F.; Liu, P.; Adzic, R. R. Highly Stable Pt Monolayer on PdAu Nanoparticle Electrocatalysts for the Oxygen Reduction Reaction. *Nat. Commun.* **2012**, *3*, 1115.
(18) Wang, J. X.; Inada, H.; Wu, L.; Zhu, Y.; Choi, Y.; Liu, P.; Zhou, W.-P.; Adzic, R. R. Oxygen Reduction on Well-Defined Core−Shell Nanocatalysts: Particle Size, Facet, and Pt Shell Thickness Effects. *J. Am. Chem. Soc.* **2009**, *131*, 17298−17302.
(19) Song, L.; Liang, Z.; Vukmirovic, M. B.; Adzic, R. R. Enhanced Oxygen Reduction Reaction Activity on Pt-Monolayer-Shell PdIr/Ni-Core Catalysts. *J. Electrochem. Soc.* **2018**, *165*, J3288−J3294.
(20) Strasser, P.; Koh, S.; Anniyev, T.; Greeley, J.; More, K.; Yu, C.; Liu, Z.; Kaya, S.; Nordlund, D.; Ogasawara, H.; Toney, M. F.; Nilsson, A. Lattice-strain Control of the Activity in Dealloyed Core-shell Fuel Cell Catalysts. *Nat. Chem.* **2010**, *2*, 454−460.
(21) Mani, P.; Srivastava, R.; Strasser, P. Dealloyed Binary PtM_3 (M=Cu, Co, Ni) and Ternary $PtNi_3M$ (M=Cu, Co, Fe, Cr) Electrocatalysts for the Oxygen Reduction Reaction: Performance in Polymer Electrolyte Membrane Fuel Cells. *J. Power Sources* **2011**, *196*, 666−673.
(22) Liu, G. C.; Stevens, D. A.; Burns, D. A.; Sanderson, R. J.; Vernstrom, G.; Atanasoski, R. T.; Debe, M. K.; Dahna, J. R. Oxygen Reduction Activity of Dealloyed $Pt_{1-x}Ni_x$ Catalysts. *J. Electrochem. Soc.* **2011**, *158*, B919−B926.
(23) Wang, Y.; Sun, D.; Chowdhury, T.; Wagner, J. S.; Kempa, T. J.; Hall, A. S. Rapid Room-Temperature Synthesis of a Metastable Ordered Intermetallic Electrocatalyst. *J. Am. Chem. Soc.* **2019**, *141*, 2342−2347.
(24) Wang, T.; Liang, J.; Zhao, Z.; Li, S.; Lu, G.; Xia, Z.; Wang, C.; Luo, J.; Han, J.; Ma, C.; Huang, Y.; Li, Q. Sub-6 nm Fully Ordered $L1_0$-Pt-Ni-Co Nanoparticles Enhance Oxygen Reduction via Co Doping Induced Ferromagnetism Enhancement and Optimized Surface Strain. *Adv. Energy Mater.* **2019**, *9*, 1803771.
(25) Xiong, Y.; Xiao, L.; Yang, Y.; DiSalvo, F. J.; Abruña, H. D. High-Loading Intermetallic Pt_3Co/C Core-Shell Nanoparticles as Enhanced Activity Electrocatalysts toward the Oxygen Reduction Reaction (ORR). *Chem. Mater.* **2018**, *30*, 1532−1539.
(26) Xiao, W.; Cordeiro, M. A. L.; Gao, G.; Zheng, A.; Wang, J.; Lei, W.; Gong, M.; Lin, R.; Stavitski, E.; Xin, H. L.; Wang, D. Atomic Rearrangement from Disordered to Ordered Pd-Fe Nanocatalysts with Trace Amount of Pt Decoration for Efficient Electrocatalysis. *Nano Energy* **2018**, *50*, 70−78.
(27) Li, J.; Xi, Z.; Pan, Y.-T.; Spendelow, J. S.; Duchesne, P. N.; Su, D.; Li, Q.; Yu, C.; Yin, Z.; Shen, B.; Kim, Y. S.; Zhang, P.; Sun, S. Fe Stabilization by Intermetallic $L1_0$-FePt and Pt Catalysis Enhancement in $L1_0$-FePt/Pt Nanoparticles for Efficient Oxygen Reduction Reaction in Fuel Cells. *J. Am. Chem. Soc.* **2018**, *140*, 2926−2932.
(28) Kuttiyiel, K. A.; Kattel, S.; Cheng, S.; Lee, J. H.; Wu, L.; Zhu, Y.; Park, G.-G.; Liu, P.; Sasaki, K.; Chen, J. G.; Adzic, R. R. Au-Doped Stable $L1_0$ Structured Platinum Cobalt Ordered Intermetallic Nanoparticle Catalysts for Enhanced Electrocatalysis. *ACS Appl. Energy Mater.* **2018**, *1*, 3771−3777.
(29) Du, X. X.; He, Y.; Wang, X. X.; Wang, J. N. Fine-grained and Fully Ordered Intermetallic PtFe Catalysts with Largely Enhanced Catalytic Activity and Durability. *Energy Environ. Sci.* **2016**, *9*, 2623−2632.
(30) Li, J.; Sharma, S.; Liu, X.; Pan, Y.-T.; Spendelow, J. S.; Chi, M.; Jia, Y.; Zhang, P.; Cullen, D. A.; Xi, Z.; Lin, H.; Yin, Z.; Shen, B.; Muzzio, M.; Yu, C.; Kim, Y. S.; Peterson, A. A.; More, K. L.; Zhu, H.;

https://dx.doi.org/10.1021/acscatal.0c03036
ACS Catal. 2020, 10, 10637−10645

Sun, S. Hard-Magnet $L1_0$-CoPt Nanoparticles Advance Fuel Cell Catalysis. *Joule* **2019**, *3*, 124−135.
(31) Xiao, W.; Lei, W.; Gong, M.; Xin, H. L.; Wang, D. Recent Advances of Structurally Ordered Intermetallic Nanoparticles for Electrocatalysis. *ACS Catal.* **2018**, *8*, 3237−3256.
(32) Qin, Y.; Luo, M.; Sun, Y.; Li, C.; Huang, B.; Yang, Y.; Li, Y.; Wang, L.; Guo, S. Intermetallic hcp-PtBi/fcc-Pt Core/Shell Nanoplates Enable Efficient Bifunctional Oxygen Reduction and Methanol Oxidation Electrocatalysis. *ACS Catal.* **2018**, *8*, 5581−5590.
(33) Kim, J.; Lee, Y.; Sun, S. Structurally Ordered FePt Nanoparticles and Their Enhanced Catalysis for Oxygen Reduction Reaction. *J. Am. Chem. Soc.* **2010**, *132*, 4996−4997.
(34) Bu, L.; Zhang, N.; Guo, S.; Zhang, X.; Li, J.; Yao, J.; Wu, T.; Lu, G.; Ma, J.-Y.; Su, D.; Huang, X. Biaxially Strained PtPb/Pt Core/Shell Nanoplate Boosts Oxygen Reduction Catalysis. *Science* **2016**, *354*, 1410−1414.
(35) Liu, M.; Xin, H.; Wu, Q. Unusual strain effect of a Pt-based L10 face-centered tetragonal core in core/shell nanoparticles for the oxygen reduction reaction. *Phys. Chem. Chem. Phys.* **2019**, *21*, 6477−6484.
(36) Kudo, D.; Kaneko, S.; Myochi, R.; Chida, Y.; Todoroki, N.; Tanabe, T.; Wadayama, T. Ligand-Effect-Induced Oxygen Reduction Reaction Activity Enhancement for Pt/Zr/Pt(111) Surfaces with Tensile Strain Relieved by Stacking Faults. *ACS Appl. Energy Mater.* **2019**, *2*, 4597−4601.
(37) Kuttiyiel, K. A.; Sasaki, K.; Choi, Y.; Su, D.; Liu, P.; Adzic, R. R. Nitride Stabilized PtNi Core-shell Nanocatalyst for High Oxygen Reduction Activity. *Nano Lett.* **2012**, *12*, 6266−6271.
(38) Ott, S.; Orfanidi, A.; Schmies, H.; Anke, B.; Nong, H. N.; Hübner, J.; Gernert, U.; Gliech, M.; Lerch, M.; Strasser, P. Ionomer Distribution Control in Porous Carbon-Supported Catalyst Layers for High-Power and Low Pt-Loaded Proton Exchange Membrane Fuel Cells. *Nat. Mater.* **2019**, *19*, 77.
(39) Park, Y.-C.; Tokiwa, H.; Kakinuma, K.; Watanabe, M.; Uchida, M. Effects of Carbon Supports on Pt Distribution, Ionomer Coverage and Cathode Performance for Polymer Electrolyte Fuel Cells. *J. Power Sources* **2016**, *315*, 179−191.
(40) Yu, J.; Yoshikawa, Y.; Matsuura, T.; Islam, M. N.; Hori, M.; Hori, M. Preparing Gas-Diffusion Layers of PEMFCs with a Dry Deposition Technique. *Electrochem. Solid-State Lett.* **2005**, *8*, A152−A323.
(41) Song, L.; Cai, Y.; Zhao, X.; Liu, Y.; Kuttiyiel, K.; Marinkovic, N.; Frenkel, A.; Kim, Y. S.; Kongkanand, A.; Choi, Y.; Adzic, R. R.; Sasaki, K. One-Step Synthesis of Highly Efficient Nitride-Stabilized PtNiN Catalyst for the Oxygen Reduction Reaction, in preparation.
(42) Dai, Z. R.; Sun, S.; Wang, Z. L. Phase Transformation, Coalescence, and Twinning of Monodisperse FePt Nanocrystals. *Nano Lett.* **2001**, *1*, 443−447.
(43) van der Vliet, D. F.; Wang, C.; Li, D.; Paulikas, A. P.; Greeley, J.; Rankin, R. B.; Strmcnik, D.; Tripkovic, D.; Markovic, N. M.; Stamenkovic, V. R. Unique Electrochemical Adsorption Properties of Pt-skin Surfaces. *Angew. Chem., Int. Ed.* **2012**, *51*, 3139−3142.
(44) Rudi, S.; Cui, C.; Gan, L.; Strasser, P. Comparative Study of the Electrocatalytically Active Surface Areas (ECSAs) of Pt Alloy Nanoparticles Evaluated by Hupd and CO-stripping Voltammetry. *Electrocatalysis* **2014**, *5*, 408−418.
(45) Lytle, F. W.; Wei, P. S. P.; Greegor, R. B.; Via, G. H.; Sinfelt, J. H. Effect of Chemical Environment on Magnitude of X-ray Absorption Resonance at L_{III} Edges. Studies on Metallic Elements, Compounds, and Catalysts. *J. Chem. Phys.* **1979**, *70*, 4849−4855.
(46) Horsley, J. A. Relationship between the Area of $L_{2,3}$ X-ray Absorption Edge Resonances and the *d* Orbital Occupancy in Compounds of Platinum and Iridium. *J. Chem. Phys.* **1982**, *76*, 1451−1458.
(47) Sasaki, K.; Marinkovic, N.; Isaacs, H. S.; Adzic, R. R. Synchrotron-Based In Situ Characterization of Carbon-Supported Platinum and Platinum Monolayer Electrocatalysts. *ACS Catal.* **2016**, *6*, 69−76.
(48) McBreen, J.; Mukerjee, S. In situ X-ray Absorption Studies of Carbon-supported Pt and Pt Alloy Nanoparticles, in *Interfacial Electrochemistry: Theory, Experimental and Applications*; Wieckowski, A., Ed.; Marcel Dekker: New York, 1999; pp 895−914.
(49) Montejano-Carrizales, J. M.; Aguilera-Granja, F.; Morán-López, J. L. Direct Enumeration of the Geometrical Characteristics of Clusters. *Nanostruct. Mater.* **1997**, *8*, 269−287.
(50) Marinkovic, N. S.; Sasaki, K.; Adzic, R. R. Determination of Single- and Multi-Component Nanoparticle Sizes by X-ray Absorption Spectroscopy. *J. Electrochem. Soc.* **2018**, *165*, J3222−J3230.
(51) Frenkel, A. I.; Stern, E. A.; Voronel, A.; Heald, S. M. Lattice Strains in Disordered Mixed Salts. *Solid State Commun.* **1996**, *99*, 67−71.
(52) Tylus, U.; Jia, Q.; Strickland, K.; Ramaswamy, N.; Serov, A.; Atanassov, P.; Mukerjee, S. Elucidating Oxygen Reduction Active Sites in Pyrolyzed Metal-Nitrogen Coordinated Non-Precious-Metal Electrocatalyst Systems. *J. Phys. Chem. C* **2014**, *118*, 8999−9008.
(53) Holby, E. F.; Zelenay, P. Linking Structure to Function: The Search for Active Sites in Non-platinum Group Metal Oxygen Reduction Reaction Catalysts. *Nano Energy* **2016**, *29*, 54−64.
(54) Serov, A.; Artyushkova, K.; Atanassov, P. Fe-N-C Oxygen Reduction Fuel Cell Catalyst Derived from Carbendazim: Synthesis, Structure, and Reactivity. *Adv. Energy Mater.* **2014**, *4*, 1301735.
(55) Bocquet, M. L.; Cerda, J.; Sautet, P. Transformation of Molecular Oxygen on a Platinum Surface: A Theoretical Calculation of STM Images. *Phys. Rev. B: Condens. Matter Mater. Phys.* **1991**, *59*, 15437−15445.
(56) Ou, L.; Yang, F.; Liu, Y.; Chen, S. First-Principle Study of the Adsorption and Dissociation of O_2 on Pt(111) in Acidic Media. *J. Phys. Chem. C* **2009**, *113*, 20657−20665.

https://dx.doi.org/10.1021/acscatal.0c03036
ACS Catal. 2020, 10, 10637−10645